Interstellar Scintillation of the Radio-Loud Magnetar XTE J1810–197

Rui Wang(王睿)[1,2], Zhen Yan(闫振)[3,1,2*], Zhiqiang Shen(沈志强)[3,1,2,4*], Zhenlong Liao(廖振龙)[1,2], Zhipeng Huang(黄志鹏)[5], Yajun Wu(吴亚军)[3,1,2], Rongbing Zhao(赵融冰)[3,1,2], Xiaowei Wang(王啸威)[1,2], Jie Liu(刘杰)[1], Kuo Liu(刘阔)[3,1,2], Fan Yang(杨帆)[1,4], Yangyang Lin(林杨洋)[1], and Chuyuan Zhang(张楚原)[1,2]

[1]*Shanghai Astronomical Observatory, Chinese Academy of Sciences, Shanghai 200030, China*
[2]*University of Chinese Academy of Sciences, Beijing 100049, China*
[3] *State Key Laboratory of Radio Astronomy and Technology, Shanghai Astronomical Observatory, Chinese Academy of Sciences, Shanghai 200030, China*
[4]*School of Physical Science and Technology, ShanghaiTech University, Shanghai 201210, China*
[5]*School of Physics and Mechanical & Electrical Engineering, Institute of Astronomy and High Energy Physics, Hubei University of Education, Wuhan 430205, China*

(Received 25 December 2025; accepted manuscript online 27 February 2026)

In this Letter, we present a comprehensive interstellar scintillation (ISS) study of the radio-loud magnetar XTE J1810–197 based on six years (2018–2024) of multifrequency monitoring (7.0, 8.6, and 14.0 GHz) with the Shanghai Tian Ma Radio Telescope. Scintillation parameters such as decorrelation bandwidth $\Delta\nu_{\rm d}$, decorrelation time $\Delta\tau_{\rm d}$, and drift rate $\mathrm{d}t/\mathrm{d}\nu$, are fully characterized by the two-dimensional auto-correlation analysis. The measured $\Delta\tau_{\rm d}$ is less than 4 s at 575–725 MHz under a Kolmogorov spectrum, which is shorter than the 5.54 s spin period of the magnetar, thereby explaining the previously reported absence of pulse-to-pulse coherence at these frequencies. Kinematic modeling is utilized to locate the dominant scattering screen 1.6 ± 0.1 kpc away from the Earth, within the Sagittarius Arm. The screen coincides with the H II region JCMTSE J180921.2–201932 and is unrelated to the 2018 outburst of the magnetar, as suggested by earlier studies. The scintillation arc detected at 14.0 GHz is the highest-frequency arc observed to date. The arc asymmetry is linearly correlated with the dispersion-measure gradient across the screen ($r = 0.959$, $p < 10^{-8}$). Further, we measure its refractive scintillation timescale, which is only 1.21 ± 0.19 d. Clear diffractive interstellar scintillation at 14 GHz effectively resolves the debate over a possible strong-to-weak scattering transition at this frequency. These results extend the ISS characterization of magnetars to previously unexplored frequencies, providing a precise probe for ionized interstellar media in the Sagittarius Arm.

DOI: 10.1088/0256-307X/43/4/041101 CSTR: 32039.14.0256-307X.43.4.041101

1. Introduction. Magnetars are a class of neutron stars distinguished by their ultrastrong magnetic fields ($B \sim 10^{14}$–10^{15} G) hundreds of times stronger than those of ordinary pulsars. Magnetars are characterized by intense sporadic X-ray and soft γ ray outbursts. The energy released in these outbursts significantly exceeds the rotational energy loss from the spin-down of the star, suggesting that their emissions are powered by the gradual decay and catastrophic restructuring of their immense magnetic fields rather than by their rotation.[1] Unlike ordinary radio pulsars, only a small proportion of magnetars exhibit detectable radio signals. Further, they exhibit transient emissions distinct from the steady pulsations of ordinary pulsars.[2] Thus far, only 30 magnetars have been discovered (24 confirmed and six candidates); six of them have been detected to emit radio pulsations.[3,4]

XTE J1810–197 (also known as PSR J1809–1943) was discovered in 2003 as an anomalous X-ray pulsar.[5] Subsequent observations identified it as the first radio-loud magnetar with a spin period $P = 5.54$ s and dispersion measure $\mathrm{DM} = 178\pm5\,\mathrm{pc\cdot cm^{-3}}$.[6,7] In late 2008, XTE J1810–197 entered a decade-long quiescent phase before the radio and X-ray outbursts in December 2018.[8,9] Although the DM of XTE J1810–197 yields distances of 3.6 and 3.1 kpc based on the NE2001[10] and YMW16 models,[11] respectively, the very long baseline array (VLBA) parallax measurements provide a closer distance of 2.5 ± 0.4 kpc.[12] Further, the VLBA observations revealed proper motion $(\mu_\omega, \mu_\delta) = (3.70, -16.13)\,\mathrm{mas\cdot yr^{-1}}$ in the barycentric ecliptic coordinate system (corresponding to a transverse velocity $V_{\rm p} \approx 200\,\mathrm{km\cdot s^{-1}}$) and scattering size of 0.7 ± 0.4 mas at 5.7 GHz. The scattering size of this pulsar confirms a strong interstellar medium (ISM) scattering effect directly associated with interstellar scintillation (ISS). Thus, XTE J1810–197 is an ideal target for investigating the ISM through ISS studies.

Shortly after the discovery of pulsars, diffractive interstellar scintillation (DISS) was proposed to explain the

*Corresponding authors. Email: yanzhen@shao.ac.cn; zshen@shao.ac.cn
© 2026 Chinese Physical Society and IOP Publishing Ltd. All rights, including for text and data mining, AI training, and similar technologies, are reserved.

flux density fluctuations in pulsars on short timescales ($\sim$ min) and narrow bandwidths ($\sim$ kHz–MHz) characterized by decorrelation time ($\Delta\tau_{\rm d}$) and decorrelation bandwidth ($\Delta\nu_{\rm d}$), respectively.[13,14] As research progressed, long-term variations in the pulsar flux density (tens of days or more) were discovered and explained through refractive interstellar scintillation (RISS).[15] The ISS observations of pulsars serve as powerful tools to investigate the structure and characteristics of the ISM, such as H II regions, supernova remnants, and nebulae.[16–18] However, very few ISS studies have focused on magnetars. The limited number of magnetars with radio pulse radiation can be attributed to their erratic radio emissions masking their tiny ISS patterns. Their relatively long spin period also limits the subintegration length. Recently, the ISS of XTE J1810–197 at 575–725 MHz was investigated systematically using the upgraded Giant Metrewave Radio Telescope (uGMRT),[19] and the $\Delta\nu_{\rm d}$ of XTE J1810–197 was measured. However, $\Delta\tau_{\rm d}$ was not acquired, suggesting that measuring $\Delta\tau_{\rm d}$ requires higher-frequency observations as $\Delta\tau_{\rm d}$ will be longer and easier to measure at higher frequencies.[20] The ISS features of XTE J1810–197 were hypothesized to be associated with the 2018 outburst and fade over time. However, evidence to test this idea remains lacking.

In this Letter, we present our ISS study results of XTE J1810–197 measured at 7.00, 8.60, and 14.0 GHz using the Shanghai Tian Ma Radio Telescope (TMRT). Detailed observation information is provided in Section 2, and relevant data analysis are presented in Section 3. The discussions are provided in Section 4, followed by the conclusions in Section 5.

2. Observations. TMRT, 65-m diameter fully steerable antenna, was built in the 2010s in the Songjiang district of Shanghai City. Equipped with eight sets of low-noise cryogenic receivers and an active surface system, the TMRT operates over a frequency range from 1.3–50.0 GHz. The digital backend system built for the TMRT includes three pairs of analog-to-digital converters and three corresponding Roach-II electronic boards.[21] We frequently monitored XTE J1810–197 throughout its active phase (2018–2024) at 8.60 GHz using TMRT and published its timing and radiation properties.[22] We selected 83 epochs of data with a long track length, high flux density, minimal radio frequency interference (RFI), and stable pulse profiles from these observations to study its ISS. Further, we incorporated six epochs of 7.00 GHz and one epoch of 14.0 GHz data with TMRT to investigate its multifrequency ISS. The observation bandwidth (BW) was 800 MHz at all three frequencies. The total BW was divided into sub-channels with typical widths of 1.95 MHz and typical sub-integration length of 30 s to mitigate dispersion and RFI.

3. Data Analysis and Results. Observational data were pre-processed as follows: Firstly, we applied bandpass calibration using standard flux calibrators (3C 286 or 3C 295). Subsequently, RFI was mitigated by excising contaminated sub-integrations and channels interactively using the `pazi` tool in PSRCHIVE.[23,24]* Subsequently, we generated preliminary dynamic spectra using the `psrflux` command. Intrinsic luminosity variations were suppressed using the `correct_dyn` function in SCINTOOLS to isolate the scintillation signal.[25,26]† This function employs singular value decomposition. The 14.0 GHz data were excluded from this correction step because of the strong intrinsic variability. Finally, any data gaps resulting from RFI mitigation were filled using linear interpolation to ensure continuity in the final dynamic spectra.

Dynamic spectra plots were employed to visualize the variations of the flux intensity with observation frequency and time. Visible scintillation structures (scintles) were observed at 7.00, 8.60, and 14.0 GHz. Following previous studies,[25,27,28] we used a two-dimensional (2D) autocorrelation function (ACF) to quantify the average characteristics of scintles ($\Delta\nu_{\rm d}$, $\Delta\tau_{\rm d}$, and frequency drift rate ${\rm d}t/{\rm d}\nu$). 2D-ACFs were fitted using a 2D exponential model with the open source package `scintools`[25,26] [detailed fitting method is provided in Appendix S2 of the Supplementary Materials (SM)]. The strength of DISS is quantified by the modulation index, which is defined as $m = \sigma_{\rm S}/\overline{S(\nu,t)}$, where $\sigma_{\rm S}$ and $\overline{S(\nu,t)}$ represent the standard deviation of the flux density S and mean of flux intensity, respectively. Further, we used the Fourier power spectrum of the dynamic spectrum of the pulsar to investigate scattering screens along the line of sight (LoS) by analyzing their parabolic arc structures. The dynamic spectrum was first resampled in the wavelength domain $S(t,\lambda)$ using SCINTOOLS to remove the frequency dependence of the arc curvature. The outer 10% of the data was tapered with a Hamming window function for mitigating sidelobe effects. Following mean subtraction and prewhitening, the secondary spectrum was derived via a 2D Fourier transform. To enhance the visibility of the arc structures, the logarithmic secondary spectrum $\mathcal{S}$ was obtained from

$$\mathcal{S}(f_t, f_\lambda) = 10\log_{10}(|\tilde{S}(t,\lambda)|^2), \tag{1}$$

where $\tilde{S}(t,\lambda)$ represents the 2D Fourier transform of the preprocessed wavelength-domain dynamic spectrum. Scintillation arcs are parameterized by their curvature η and half-width w. The arc regions are defined by the inequality $|f_\lambda - \eta f_t^2| < w$, where f_t and f_λ represent the Fourier conjugates of the time t and wavelength λ axes, respectively. Parameters η and w are determined using a Hough-transform-based fitting method.[29]

At 8.60 GHz, $\Delta\tau_{\rm d}$ was in the range of 0.85–1.80 min, with a mean of 1.22 min. This was approximately twice the time resolution of our data. $\Delta\nu_{\rm d}$ was in the range of 4.2–13.5 MHz, averaging 8.1 MHz. The DISS modulation index m ranged irregularly between 0.49 and 1.38, and therefore, the ISS of this magnetar remained in the strong regime. These parameters exhibited no systematic evolution over

*http://psrchive.sourceforge.net/
†https://github.com/danielreardon/scintools

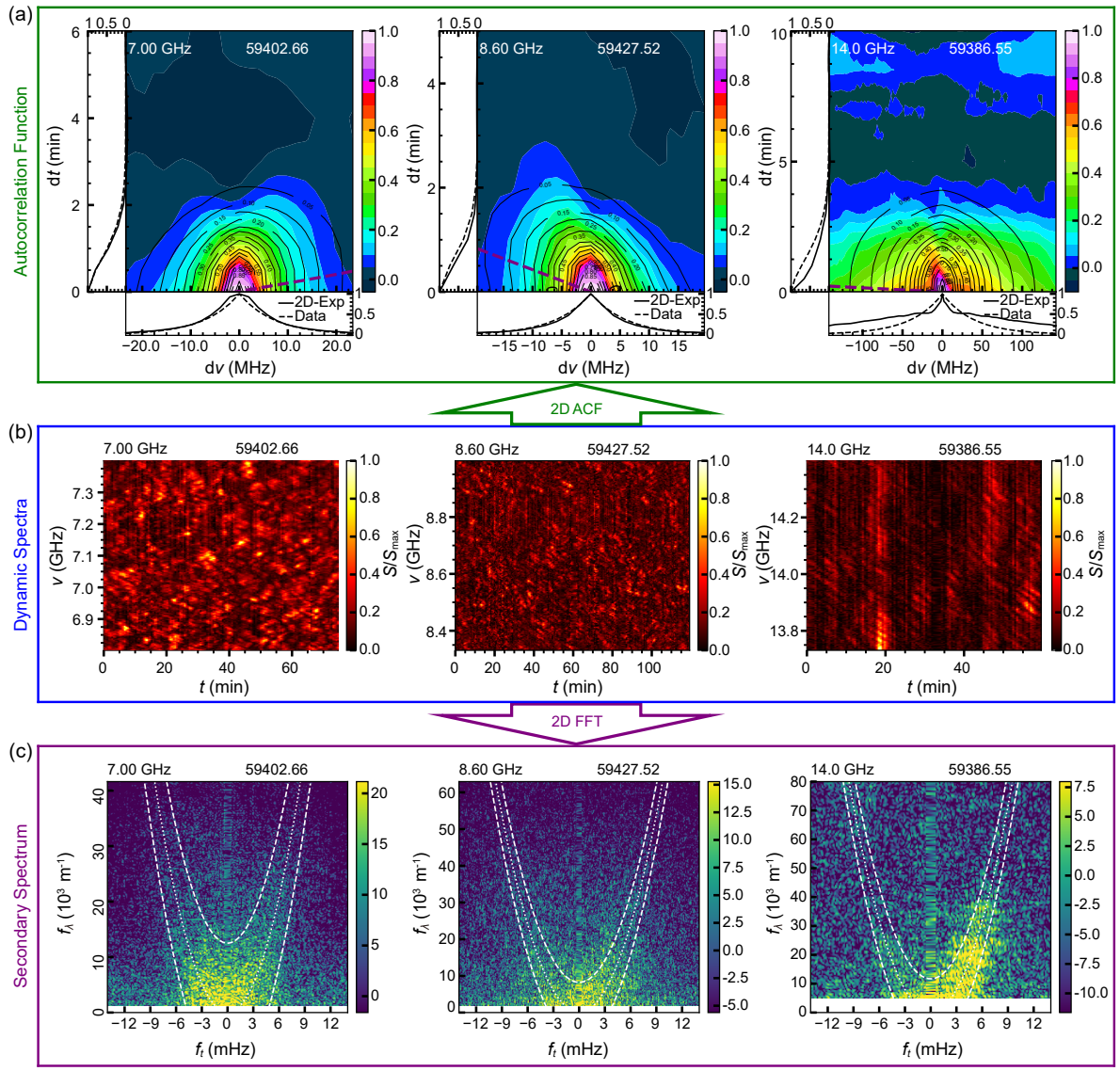

Fig. 1. Representative plots of ISS data analysis results for observations listed in Table 1. (a) 2D-ACFs: The normalized 2D-ACFs are presented with color-filled contours (scaled with the color-bar on the right), and the 2D-exponential form fitting results are presented as black-line contours. The major axis is marked with the dashed line. The bottom and left sub-panels are the one-dimensional cuts of the 2D-ACF (solid curves) and best-fit model (dashed curves) at zero time and frequency lag. (b) Dynamic spectra: The intensity of each pixel is scaled linearly with the color bar on the right. (c) Secondary spectra: White dashed and dotted curves represent the boundaries and center of the best-fit arc regions, respectively.

Table 1. Information and results of our representative ISS observations at each frequency: observation frequency (ν), modified Julian date (MJD), observation length (T), decorrelation bandwidth ($\Delta\nu_{\rm d}$), decorrelation time ($\Delta\tau_{\rm d}$), drift rate ($\mathrm{d}t/\mathrm{d}\nu$), curvature of arc ($\eta$), half-width of arc ($w$), logarithmic asymmetry of arc ($\ln(S_{\rm r}/S_{\rm l})$), reduced ISS speed ($V_{\rm iss,0}$), DM gradient ($\partial\mathrm{DM}/\partial t$), DISS modulation index (m), and their 1-σ uncertainties (if measured). The complete table is presented as Table S1 in the SM.

ν (GHz)	MJD	T (s)	$\Delta\nu_{\rm d}$ (MHz)	$\Delta\tau_{\rm d}$ (min)	$\mathrm{d}t/\mathrm{d}\nu$ (s/MHz)	η ($\mathrm{m^{-1}\cdot mHz^{-2}}$)	w (10^3 $\mathrm{m^{-1}}$)	$\ln(S_{\rm r}/S_{\rm l})$	$V_{\rm iss,0}$ ($\mathrm{km\cdot s^{-1}}$)	$\partial\mathrm{DM}/\partial t$ ($\mathrm{pc\cdot cm^{-3}\cdot yr^{-1}}$)	m
7.00	59402.65	4480	4.95±0.12	1.22±0.03	1.15±0.07	573^{+42}_{-29}	$12.7^{+1.1}_{-2.8}$	$-0.12^{+0.01}_{-0.01}$	261±22	−0.05±0.01	0.67
8.60	59427.50	7155	4.23±0.07	1.01±0.02	−2.66±0.08	661^{+55}_{-25}	$7.8^{+2.3}_{-1.5}$	$0.35^{+0.01}_{-0.03}$	238±20	0.16±0.01	0.77
14.0	59386.52	3578	27.96±1.90	1.97±0.13	−0.09±0.03	881^{+100}_{-22}	$11.6^{+1.2}_{-3.0}$	$1.48^{+0.04}_{-0.03}$	194±21	0.02±0.01	0.92

time. The values of $\Delta\tau_{\rm d}$ and $\Delta\nu_{\rm d}$ for the 7.00 GHz observation were smaller than those for 8.60 GHz, while m was similar. The only 14.0 GHz observation was influenced by strong intrinsic variability. Detailed discussions have been presented in Section 4. Representative dynamic spectra, 2D-ACFs, and secondary spectra for each observation frequency are presented in Fig. 1, and the corresponding ISS analysis results are listed in Table 1. The complete set

of plots and detailed data table for all observations are provided in the SM (Appendices S1–S3 and Table S1, respectively).

4. Discussions.

4.1 Comparison with Previous Studies. Marthi and Maan [19] conducted ISS observations of XTE J1810–197 using the uGMRT. They measured $\Delta\nu_{\rm d}$ in the 575–725 MHz band and predicted that $\Delta\tau_{\rm d}$ would be in the range of 6.9–9.4 s at these frequencies according to the NE2001 model. [10] However, an attempt to constrain it from the cross-correlation of pulses failed. Extrapolating our measurements of $\Delta\tau_{\rm d}$ to 575–725 MHz (assuming it follows a Kolmogorov spectrum $\Delta\tau_{\rm d} \propto \nu^{1.2}$ [20]) gives $\Delta\tau_{\rm d} < 4$ s, which is shorter than the 5.54 s spin period. This accounts for the absence of pulse-to-pulse coherence at those frequencies. Further, they examined the frequency dependence of $\Delta\nu_{\rm d}$, which follows $\Delta\nu_{\rm d} \propto \nu^{\alpha}$. [20] Their analysis yielded a best-fit $\alpha = 4.0 \pm 0.3$; however, the Kolmogorov spectrum ($\alpha = 4.4$) was consistent with their data, and consequently, they concluded consistency with the Kolmogorov turbulence. Extrapolating their result to 8.60 GHz yields $\Delta\nu_{\rm d} \approx 11.9 \pm 0.6$ MHz (for $\alpha = 4.4$) or 4.23 ± 0.22 MHz (for $\alpha = 4.0$). Both extrapolations were consistent with our direct measurement from 4.2 to 13.5 MHz. This study also hypothesized that the ISS was associated with the 2018 outburst and would diminish over time; however, our six-year monitoring campaign found no such evolution.

In contrast to the predicted strong-to-weak ISS transition at 14.6 GHz with $\Delta\nu_{\rm d} \simeq 320$ MHz, [30] the extrapolation of uGMRT observations yields $\Delta\nu_{\rm d} \simeq 32$ MHz at 14 GHz, which is nearly one order of magnitude smaller. [19] We only have one ISS observation at 14.0 GHz (MJD 59386.52). The analysis was conducted on uncorrected data because of strong intrinsic variability, which appeared as vertical stripes in the dynamic spectrum and as a ridge at $\Delta\tau \approx 0$ in the 2D-ACF (Fig. 1). Consequently, the derived $\Delta\nu_{\rm d} = 27.96 \pm 1.90$ MHz might have been overestimated. However, this value agreed with the extrapolation of uGMRT observations [19] and was significantly lower than the theoretical prediction, [30] challenging the predicted strong-to-weak transition scenario. This conclusion was supported by $m \approx 1$ at 14.0 GHz, which indicated a strong ISS at this frequency.

4.2 Location of the Scattering Screen. The ISS speed $V_{\rm iss}$ is defined as the velocity of the diffraction pattern relative to the observer. For a thin screen at a distance of $L_{\rm o}$ from the observer and $L_{\rm p}$ from the pulsar, with a total distance of $D = L_{\rm o} + L_{\rm p}$, $V_{\rm iss}$ is given by

$$V_{\rm iss} = A_0 \frac{\sqrt{\Delta\nu_{\rm d} D x}}{\nu \Delta\tau_{\rm d}} = \sqrt{x} V_{\rm iss,0}, \tag{2}$$

where $x = L_{\rm o}/L_{\rm p}$ represents the fractional screen distance. The quantity $V_{\rm iss,0} = A_0\sqrt{\Delta\nu_{\rm d} D}/(\nu\Delta\tau_{\rm d})$ represents the reduced ISS speed. The model-dependent constant $A_0 = 3.85 \times 10^4$ [31] yields $V_{\rm iss}$ in km · s^{-1} when the input parameters $\Delta\nu_{\rm d}$, D, ν, and $\Delta\tau_{\rm d}$ are in the units of megahertz, kiloparsec, gigahertz, and seconds, respectively.

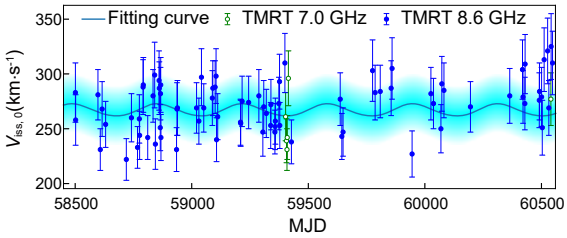

Fig. 2. Observed $V_{\rm iss,0}$ and fitting curve. $V_{\rm iss,0}$ at 7.0 and 8.6 GHz and their 1-σ error ranges marked with hollow green and solid blue points with error bars. The blue curve with a shaded region is the fitting curve and its 1-σ error ranges.

ISS velocity $\boldsymbol{V}_{\rm iss}$ is modeled as a weighted vector combination of the transverse proper motion ($\boldsymbol{V}_{\rm p,\perp}$ of the pulsar, where $\perp$ represents the component perpendicular to the LoS); the orbital velocity of the Earth ($\boldsymbol{V}_{\rm Earth,\perp}$); and the transverse velocity of the scattering screen ($\boldsymbol{V}_{\rm scr,\perp}$).

$$\boldsymbol{V}_{\rm iss} = x\boldsymbol{V}_{\rm p,\perp} + \boldsymbol{V}_{\rm Earth,\perp} - (1+x)\boldsymbol{V}_{\rm scr,\perp}. \tag{3}$$

For an isolated pulsar, $\boldsymbol{V}_{\rm p,\perp}$ and $\boldsymbol{V}_{\rm scr,\perp}$ can be treated as constants over multiyear timescales. [32,33]

The observed $V_{\rm iss,0}$ for XTE J1810–197 showed substantial scatter, preventing a complete fit. Therefore, we adopted the common simplification of a stationary scattering screen ($\boldsymbol{V}_{\rm scr,\perp} = 0$), which is justified when the transverse speed of the pulsar significantly exceeds that of the screen. [31] Under this assumption, for a solitary pulsar at coordinates $(\omega_{\rm p}, \delta_{\rm p})$ with proper motion (μ_ω, μ_δ) in mas · yr^{-1} in barycentric ecliptic coordinates, [18,34]

$$\begin{aligned} x V_{\rm iss,0}^2 = {} & [4.74 x D \mu_\omega - V_{\rm e}\cos(\omega_{\rm e} - \omega_{\rm p})]^2 \\ & + [4.74 x D \mu_\delta - V_{\rm e}\sin\delta_{\rm p}\sin(\omega_{\rm e} - \omega_{\rm p})]^2, \end{aligned} \tag{4}$$

where $V_{\rm e}$ and $\omega_{\rm e}$ represent the orbital speed and ecliptic longitude of the Earth, respectively. A least-squares fit of $V_{\rm iss,0}$ yielded $x = 1.8 \pm 0.4$. This fitting result indicated that the variation of $V_{\rm iss,0}$ from the revolution of the Earth was smaller than 11 km · s^{-1}, which is comparable to the measurement uncertainties of $V_{\rm iss,0}$, while $\boldsymbol{V}_{\rm p,\perp}$ was approximately 200 km · s^{-1}. Consequently, $V_{\rm iss,0}$ was dominated by $V_{\rm p,\perp}$, which resulted in a less prominent variation in $V_{\rm iss,0}$. Figure 2 displays an imperfect fit curve; however, it matches most $V_{\rm iss,0}$ within the error range, and therefore, $x = 1.8 \pm 0.4$ is acceptable. Using a VLBA parallax distance of $D = 2.5 \pm 0.4$ kpc, [12] $x = 1.8 \pm 0.4$ corresponds to $L_{\rm o} = 1.6 \pm 0.1$ kpc, and $L_{\rm p} = 0.9 \pm 0.1$ kpc.

The derived $L_{\rm o} = 1.6 \pm 0.1$ kpc places the scattering screen within the Sagittarius Arm, far from the magnetar but near the foreground H II region JCMTSE J180921.2–201932. This H II region located at a distance of $d_{\rm H} = 1.56$ kpc and with a projected separation of $d_{\rm H,\perp} \approx 16$ pc from the LoS to XTE J1810–197 [35] is an active high-mass star formation region. [36] This localized ionization can result in a higher local electron density than that predicted by traditional galactic electron density models. This provides a natural explanation for why both the NE2001 [10] and YMW16 [11] models overestimate the distance to XTE J1810–197. Further, this location indicates that the observed ISS is dominated by the ISM along the

LoS rather than by the local environment of the magnetar, excluding any association with the 2018 outburst. In addition, our assumption of a stationary screen is consistent with the galactic differential rotation model,[37] which predicts the transverse speed $< 0.2\,\mathrm{km\cdot s^{-1}}$ of this screen.

4.3 Curvature of Arc. The curvature η of the parabolic arc in the secondary spectrum is determined by the screen geometry and velocity of the point on the screen intersected by the LoS to the pulsar $\boldsymbol{V}_{\mathrm{eff},\perp}$. According to the anisotropic thin-screen model,[38]

$$\eta = \frac{Dx/(1+x)^2}{2(\boldsymbol{V}_{\mathrm{eff},\perp}\cdot\boldsymbol{a})^2}, \tag{5}$$

where the unit vector $\boldsymbol{a}$ signifies the orientation of the major axis of the scattering image. This is the sky projection of the underlying turbulence anisotropy.[39] Isotropic scattering occurs in the specific case where $\boldsymbol{a}$ is always parallel to $\boldsymbol{V}_{\mathrm{eff},\perp}$.

The effective transverse velocity $\boldsymbol{V}_{\mathrm{eff},\perp}$ is a weighted combination of the transverse velocities of the Earth, pulsar, and scattering screen:[38,40]

$$\boldsymbol{V}_{\mathrm{eff},\perp} = \frac{x}{1+x}\boldsymbol{V}_{\mathrm{p},\perp} + \frac{1}{1+x}\boldsymbol{V}_{\mathrm{Earth},\perp} - \boldsymbol{V}_{\mathrm{scr},\perp}. \tag{6}$$

We project $\boldsymbol{V}_{\mathrm{eff},\perp}$ onto the ecliptic coordinate system to yield components $V_{\mathrm{eff},\omega}$ (ecliptic longitude) and $V_{\mathrm{eff},\delta}$ (ecliptic latitude). Let ψ_0 be the position angle of the major axis of the scattered image measured clockwise from the ecliptic latitude direction, $\boldsymbol{a} = (\cos\psi_0, \sin\psi_0)$. Substituting this into Eq. (5) yields[18]

$$\eta = \frac{Dx/(1+x)^2}{2(V_{\mathrm{eff},\omega}\cos\psi_0 + V_{\mathrm{eff},\delta}\sin\psi_0)^2}. \tag{7}$$

Figure 3 presents the best-fit curves for the isotropic (blue) and anisotropic (green) scattering models, overlaid on the measured η from our 7.00 (yellow diamonds), 8.60 (pink diamonds), and 14.0 GHz (purple diamond) observations. Both models provide comparable fits. This degeneracy originates from the screen geometry and velocity dominance: with $x = 1.8 \pm 0.4$ and $V_{\mathrm{p},\perp} \gg V_{\mathrm{Earth},\perp}$, the effective velocity $\boldsymbol{V}_{\mathrm{eff}}$ is dominated by the motion of the pulsar. Consequently, $\boldsymbol{V}_{\mathrm{eff}}$ remains constant in both magnitude (variations $< 4\%$) and direction (deviating $< 8^\circ$ from $\boldsymbol{V}_{\mathrm{p},\perp}$). Under these conditions, anisotropic scattering behaves similar to isotropic scattering when the major axis is aligned with $\boldsymbol{V}_{\mathrm{p},\perp}$. Our anisotropic fit yields a small misalignment ($< 15^\circ$) between the major axis [$\psi_0 = (91.2 \pm 2.6)^\circ$] and $\boldsymbol{V}_{\mathrm{p},\perp}$ ($\psi_{V_\mathrm{p}} \approx 102^\circ$, wherein ψ_{V_p} represents the position angle of the line of $\boldsymbol{V}_{\mathrm{p},\perp}$ measured clockwise from the ecliptic latitude direction). We conclude that, for our current precision in η measurements, the difference between isotropic and anisotropic scattering is drowned in noise, indicating no prominent trends for distinguishing them.

4.4 Asymmetric Arcs. The parabolic arcs in the secondary spectra exhibit significant asymmetry. This feature can arise from a DM-gradient across the scattering screen[27,38] or from a physically finite screen extent.[39]

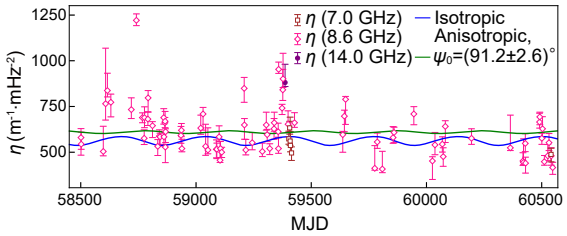

Fig. 3. Changes in η values with observation time. η at 7.00, 8.60, and 14.0 GHz and their 1-σ error ranges are indicated by hollow brown squares, hollow deep pink diamonds, and solid purple points with asymmetric error bars, respectively. The best-fit curves for isotropic (blue) and anisotropic (green) scattering scenarios are presented on the plots.

We quantified this asymmetry using the logarithmic arc asymmetry ratio, which is defined as $\ln(S_\mathrm{r}/S_\mathrm{l})$, where S_r and S_l are the integrated powers in the right ($f_t > 0$) and left ($f_t < 0$) halves of the arc region ($|f_\lambda - \eta f_t^2| < w$), respectively.

To identify the physical origin of the arc asymmetry, we calculated the dispersion measure gradient along the direction of $\boldsymbol{V}_{\mathrm{eff},\perp}$, $\partial\mathrm{DM}/\partial t$, using the following relationship[25] to determine if the DM gradient is associated with the asymmetry of the arcs:

$$\frac{\partial \mathrm{DM}}{\partial t} = -\left(\frac{\mathrm{d}t}{\mathrm{d}\nu}\right)\left(\frac{\pi\nu^3 V_{\mathrm{iss},0}^2}{c^2 D r_\mathrm{e}}\right), \tag{8}$$

where r_e represents the classical electron radius and c represents the speed of light.

Figure 4(a) shows a clear synchronous evolution of $\partial\mathrm{DM}/\partial t$ and $\ln(S_\mathrm{r}/S_\mathrm{l})$ at 8.60 GHz. The observed variation in $\partial\mathrm{DM}/\partial t$ across epochs confirms inhomogeneities within the scattering screen on a small scale. Figure 4(b) displays a highly significant linear correlation between $\partial\mathrm{DM}/\partial t$ and $\ln(S_\mathrm{r}/S_\mathrm{l})$: $\ln(S_\mathrm{r}/S_\mathrm{l}) = (2.76\pm0.09)\cdot\partial\mathrm{DM}/\partial t$, Pearson correlation coefficient $r = 0.959$, $p < 10^{-8}$. This robust relationship suggests a causal connection between the DM gradient and arc asymmetry. Therefore, we favor the interpretation that the DM-gradient within the scattering screen is the dominant cause of the observed arc asymmetry. In future, a more refined structural analysis can be conducted using very long baseline interferometry (VLBI) ISS observations.[41]

4.5. Refractive Scintillation. The long term flux density (F) variations of XTE J1810–197[22] include the RISS component, and therefore, we analyzed the RISS behavior using the 8.6 GHz monitoring data. The theoretical RISS timescale τ_r was estimated to be $\tau_\mathrm{r} = \nu\Delta\tau_\mathrm{d}/\Delta\nu_\mathrm{d}$. Using the average $\Delta\tau_\mathrm{d}$ and $\Delta\nu_\mathrm{d}$ obtained from our measurements, we determined that $\tau_\mathrm{r} \approx 0.90$ d.[42] We calculated and fitted the structure function $D(\tau)$[43] to quantify the RISS properties by saturation level D_∞, structure index α_r, characteristic timescale τ_ch, noise level D_0, and $\tau_\mathrm{r} = (\ln 2)^{1/\alpha_\mathrm{r}}\tau_\mathrm{ch}$.[44,45] However, the long-term intrinsic F evolution of the magnetar severely affected $D(\tau)$, thereby leading to a poor fit (Fig. 5(a)). To suppress slow trends, we applied a moving average filter with a window length of 250 d (τ_r estimated from the unfiltered F). After filtering,

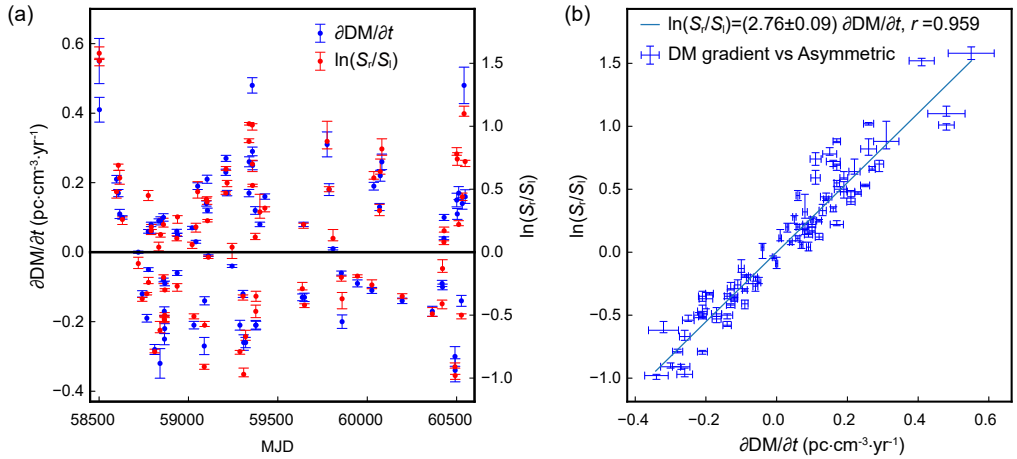

Fig. 4. $\ln(S_\mathrm{r}/S_\mathrm{l})$ and $\partial\mathrm{DM}/\partial t$ of XTE J1810–197 at 8.60 GHz. (a) displays how $\partial\mathrm{DM}/\partial t$ and $\ln(S_\mathrm{r}/S_\mathrm{l})$ varied with time. $\ln(S_\mathrm{r}/S_\mathrm{l})$, $\partial\mathrm{DM}/\partial t$, and their 1-$\sigma$ error ranges are marked with red and blue points with error bars, respectively. (b) displays the linear relationship between $\ln(S_\mathrm{r}/S_\mathrm{l})$ and $\partial\mathrm{DM}/\partial t$. We use crossing error bars to mark the 1-σ error ranges of $\ln(S_\mathrm{r}/S_\mathrm{l})$ and $\partial\mathrm{DM}/\partial t$.

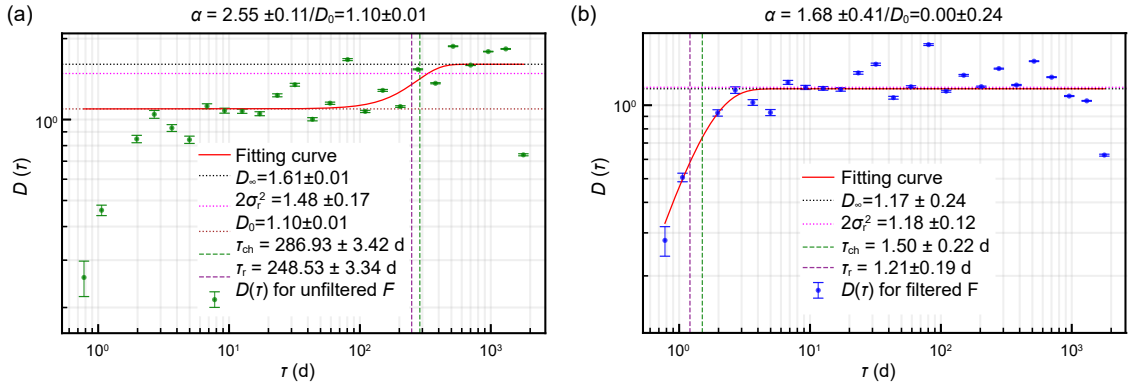

Fig. 5. $D(\tau)$ and fitting results. $D(\tau)$ and their 1-σ error ranges for unfiltered and filtered F are plotted by green and blue dots with error bars in (a) and (b), respectively. The red curve is the fitting result. Green and purple dashed lines represent τ_ch and τ_r, respectively. Black and magenta dotted lines represent D_∞ and $2\sigma_\mathrm{r}^2$, respectively, where σ_r is the RISS modulation index. For a reliable fitting, $D_\infty \approx 2\sigma_\mathrm{r}^2$. The brown dotted line indicates D_0. When D_0 is close to zero, we do not plot it.

the fit improves significantly and yields $\tau_\mathrm{r} \approx 1.21 \pm 0.19$ d (Fig. 5(b)), which is slightly larger than the theoretical estimate of 0.90 d. The complete procedure for calculating and fitting $D(\tau)$ is detailed in the Appendix 4 of the SM. τ_r is close to the shortest cadence between our observations; this can lead to an overestimation.

5. Conclusion. Through a six-year multifrequency monitoring campaign (December, 2018–September, 2024), we performed the first comprehensive analysis of the ISS from the radio-loud magnetar XTE J1810–197. We combined TMRT observations at 7.00, 8.60, and 14.0 GHz and obtained a complete set of ISS parameters ($\Delta\nu_\mathrm{d}$, $\Delta\tau_\mathrm{d}$, and $\mathrm{d}t/\mathrm{d}\nu$) that fully characterize the ISS behavior. Extrapolating our measurements to the 575–725 MHz band yielded $\Delta\tau_\mathrm{d} < 4$ s, which was shorter than the spin period ($P = 5.54$ s), explaining the absence of pulse-to-pulse coherence.[19] Kinematic modeling located the scattering screen in the Sagittarius Arm at $L_\mathrm{o} = 1.6 \pm 0.1$ kpc, which was close to the H II region JCMTSE J180921.2–201932. This screen ruled out the association between the observed ISS and the 2018 outburst of the magnetar. We detected a scintillation arc at 14.0 GHz (highest-frequency arc observed to date), surpassing the previous record of 8.60 GHz.[18] A strong linear correlation between $\ln(S_\mathrm{r}/S_\mathrm{l})$ and $\partial\mathrm{DM}/\partial t$ ($r = 0.959$, $p < 10^{-8}$) confirmed that the DM gradient across the screen was the primary cause of arc asymmetry. Further, we estimated that $\tau_\mathrm{r} = 1.21 \pm 0.19$ d at 8.60 GHz.

Our study significantly expanded the ISS characterization of XTE J1810–197 to higher frequencies; however, it found no evidence of the predicted strong-to-weak scattering transition up to 14.0 GHz.[30] Future observations at frequencies above 15 GHz may directly determine the transition frequency. Further, the discrepancy between the VLBA parallax distance and DM-derived distance confirmed that the current galactic electron density models systematically underestimated the electron densities along the LoS of XTE J1810–197.

Acknowledgments. This work was supported in part by the National SKA Program of China (Grant No. 2020SKA0120104), the National Key R&D Program of China (Grant No. 2022YFA1603104), and the

National Natural Science Foundation of China (Grant Nos. U2031119 and 12041301). We would like to express our appreciation to the anonymous referees for their constructive comments and suggestions, which were very helpful in improving this manuscript.

References

[1] Duncan R C and Thompson C 1992 *Astrophys. J. Lett.* **392** L9
[2] Camilo F, Ransom S M, Halpern J P *et al.* 2016 *Astrophys. J.* **820** 110
[3] Olausen S A and Kaspi V M 2014 *Astrophys. J. Suppl. S* **212** 6
[4] McGill Online Magnetar Catalog https://www.physics.mcgill.ca/∼pulsar/magnetar/main.html.
[5] Ibrahim A I, Markwardt C B, Swank J H *et al.* 2004 *Astrophys. J. Lett.* **609** L21
[6] Halpern J P, Gotthelf E V, Becker R H, Helfand D J, and White R L 2005 *Astrophys. J. Lett.* **632** L29
[7] Camilo F, Ransom S M, Halpern J P, Reynolds J, Helfand D J, Zimmerman N, and Sarkissian J 2006 *Nature* **442** 892
[8] Gotthelf E V, Halpern J P, Alford J A J *et al.* 2019 *Astrophys. J. Lett.* **874** L25
[9] Levin L, Lyne A G, Desvignes G, Eatough R P, Karuppusamy R, Kramer M, Mickaliger M, Stappers B W, and Weltevrede P 2019 *Mon. Not. R. Astron. Soc.* **488** 5251
[10] Cordes J M and Lazio T J W 2002 arXiv:astro-ph/0207156
[11] Yao J M, Manchester R N, and Wang N 2017 *Astrophys. J.* **835** 29
[12] Ding H, Deller A T, Lower M E, Flynn C, Chatterjee S, Brisken W Hurley-Walker N, Camilo F, Sarkissian J, and Gupta V 2020 *Mon. Not. R. Astron. Soc.* **498** 3736
[13] Scheuer P A G 1968 *Nature* **218** 920
[14] Rickett B J 1969 *Nature* **221** 158
[15] Rickett B J, Coles W W A, and Bourgois G 1984 *Astronom. Astrophys.* **134** 390
[16] Mall G, Main R A, Antoniadis J *et al.* 2022 *Mon. Not. R. Astron. Soc.* **511** 1104
[17] Yao J, Zhu W, Manchester R N *et al.* 2021 *Nature Astronomy* **5** 788
[18] Wang R, Yan Z, Shen Z, Lee K, Wu Y, Zhao R, Huang Z, Wang X, and Liu J 2025 *Sci. China Phys. Mech. Astron.* **68** 239512
[19] Marthi V R and Maan Y 2025 *Astrophys. J. Lett.* **989** L34
[20] Rickett B J 1977 *Annu. Rev. Astron. Astrophys.* **15** 479
[21] Yan Z, Shen Z, Manchester R N *et al.* 2018 *Astrophys. J.* **856** 55
[22] Huang Z P, Yan Z, Shen Z Q, Tong H, Yuan J P, Lin L, Zhao R B, Wu Y J, Liu J, Wang R, and Wang X W 2023 *Astrophys. J.* **956** 93
[23] Hotan A W, van Straten W, and Manchester R N 2004 *Publ. Astron. Soc. Aust.* **21** 302
[24] van Straten W, Demorest P, and Oslowski S 2012 *Astronomical Research and Technology* **9** 237
[25] Reardon D J and Coles W A 2023 *Mon. Not. R. Astron. Soc.* **521** 6392
[26] Reardon D J, Coles W A, Bailes M *et al.* 2020 *Astrophys. J.* **904** 104
[27] Rickett B J, Coles W A, Nava C F, McLaughlin M A, Ransom S M, Camilo F, Ferdman R D, Freire P C C, Kramer M, Lyne A G, and Stairs I H 2014 *Astrophys. J.* **787** 161
[28] Reardon D J, Coles W A, Hobbs G, Ord S, Kerr M, Bailes M, Bhat N D R, and Venkatraman Krishnan V 2019 *Mon. Not. R. Astron. Soc.* **485** 4389
[29] Xu Y H, Lee K J, Hao L F *et al.* 2018 *Mon. Not. R. Astron. Soc.* **476** 5579
[30] Lazaridis K, Jessner A, Kramer M, Stappers B W, Lyne A G, Jordan C A, Serylak M, and Zensus J A 2008 *Mon. Not. R. Astron. Soc.* **390** 839
[31] Gupta Y 1995 *Astrophys. J.* **451** 717
[32] Cordes J M and Rickett B J 1998 *Astrophys. J.* **507** 846
[33] Xu Y, Shi X, Lee K *et al.* 2023 *Mon. Not. R. Astron. Soc.* **526** 1246
[34] Bogdanov S, Pruszyńska M, Lewandowski W, and Wolszczan A 2002 *Astrophys. J.* **581** 495
[35] Contreras Y, Schuller F, Urquhart J S *et al.* 2013 *Astronom. Astrophys.* **549** A45
[36] Yang W, Gong Y, Menten K M, Urquhart J S, Henkel C and Wyrowski F Csengeri T, Ellingsen S P, Bemis A R, and Jang J 2023 *Astronom. Astrophys.* **675** A112
[37] Mróz P, Udalski A, Skowron D M *et al.* 2019 *Astrophys. J. Lett.* **870** L10
[38] Cordes J M, Rickett B J, Stinebring D R, and Coles W A 2006 *Astrophys. J.* **637** 346
[39] Shi X 2021 *Mon. Not. R. Astron. Soc.* **508** 125
[40] Stinebring D R, McLaughlin M A, Cordes J M *et al.* 2001 *Astrophys. J. Lett.* **549** L97
[41] Yan Z, Shen Z, Jiang P *et al.* 2024 *Chin. Phys. Lett.* **41** 117501
[42] Lorimer D R and Kramer M 2004 *Handbook of Pulsar Astronomy* vol.4 (Cambridge, UK: Cambridge University Press)
[43] Gitika P, Bailes M, Shannon R M *et al.* 2023 *Mon. Not. R. Astron. Soc.* **526** 3370
[44] Kaspi V M and Stinebring D R 1992 *Astrophys. J.* **392** 530
[45] Rickett B J and Lyne A G 1990 *Mon. Not. R. Astr. Soc.* **244** 68